*Journal of Applied Fluid Mechanics*, Vol. 16, No. 11, pp. 2219-2234, 2023.
Available online at www.jafmonline.net, ISSN 1735-3572, EISSN 1735-3645.
https://doi.org/10.47176/jafm.16.11.1961

# Numerical Study of High-Speed Vertical Water Entry of Hollow Projectiles with Different Aperture Sizes and Velocities

H. W. Fan[1], Z. G. Huang[1†], H. Wang[1], Z. H. Chen[1], X. Y. Liu[1], F. J. Xiao[2] and R. X. Qiu[2]

[1] *National Key Laboratory of Transient Physics, Nanjing University of Science and Technology 1, Nanjing 210094, China*
[2] *School of mechanical engineering, Nanjing University of Science and Technology, Nanjing 210094, China*

†*Corresponding Author Email: hzgkeylab@njust.edu.cn*

## ABSTRACT

The hollow projectile is a new type of projectile that has complex water entry hydrodynamics characteristics and has attracted significant attention in recent years. As such, it is important to investigate the effects of different entry velocities and aperture diameters on the cavity morphology, cavitation, dynamics, and motion characteristics of hollow projectiles when entering water at high speeds. In this study, four stages of an open cavity, cavity stretching, cavity closure, and cavity contraction in the water entry processes of a hollow projectile at 50–200 m/s and four aperture diameter projectiles at 100 m/s were studied using the volume of fluid (VOF), realizable *k-ε* turbulence, and Schnerr-Sauer cavitation model. With an increase in the speed, the depth of the cavity closure increases, thereby advancing the closure time. The timing of the surface closure at 50 m/s is clearly different from that at 100–200 m/s. Cavitation is not obvious and is near the cavity wall at 50 m/s, although the entire cavity is almost filled with vapor at 100–200 m/s. The friction resistance has two step points when impacting the water surface and entering the water completely. As the velocity increases or the aperture ratio reduces, the splash is higher, the cavity volume is larger, the cavitation phenomenon is more obvious, the cavity closure time is delayed, and the frictional resistance of the projectile is greater. The results of this study can guide the production and application of hollow projectiles in the future.

***Article History***

*Received April 28, 2023*
*Revised May 21, 2023*
*Accepted July 22, 2023*
*Available online September 3, 2023*

***Keywords:***

*Hollow projectile*
*High-speed water entry*
*Cavity shape*
*Fluid dynamics*
*Numerical calculation*

## 1. INTRODUCTION

With the development of strategic military weapons, high-speed underwater weapons have become a research priority for countries worldwide. To maintain the integrity of the national maritime domain and rapidly promote new military changes, underwater confrontations are becoming increasingly intense and heading towards systematization (Xie et al., 2019). Current research on water entry projectiles is mainly based on different solid bodies. However, hollow projectiles are lighter in mass than solid projectiles of the same caliber and have less tail vortex drag and a higher firing muzzle velocity at the same charge (Wang, 1996). They have a special structure with a coaxial through-hole and considerably less aerodynamic drag than solid projectiles (Huang et al., 2013; Zhao et al., 2019). Erfanian and nbarsooz (2018) preliminarily revealed the underwater drag reduction effect of hollow structure cavitators, wherein the drag coefficient was more than 30% smaller than that of solid discs when the aperture diameter was 0.6 times the outer diameter. Additionally, hollow projectiles have an excellent high hitting accuracy and a strong penetrating capability, which enable them to have a wide range of application prospects in underwater defense.

The water entry problem is an extremely complex, transient, and time-varying process involving the coupling of solid, liquid, and vapor phases. Here, the main focus is on spheres and projectiles of different shapes entering water. Worthington and Cole (1897) were the first to research spheres when they conducted an experimental study of water entry processes of droplets and spheres. Yun et al. (2020) conducted an experimental study on the water entry process of two spheres simultaneously. The influence of the water entry cavity and spatter formed by the first sphere on the water entry process of the second sphere was analyzed. Wang & Lyu (2021) conducted an experimental study on the parallel water entry process of two spheres. The evolution of the water entry cavity and the trajectory of the spheres were affected by the change

**NOMENCLATURE**

| | | | |
|---|---|---|---|
| $C_\mu$ | empirical constant | $\alpha_w$ | liquid phase volume fraction |
| $D$ | hollow projectile diameter | $\alpha_{nuc}$ | volume fraction of non-condensable gas |
| $d$ | hollow projectile inner diameter | $\alpha_q$ | volume fraction of phase q |
| $E_a$ | total energy of air | $\varepsilon$ | turbulent dissipation rate |
| $E_m$ | energy of mixed medium | $\mu$ | viscosity of the mixture |
| $E_w$ | total energy of water | $\vec{\mu}$ | average velocity of the mixture |
| $G_b$ | turbulent energy caused by buoyancy | $\mu_a$ | kinetic viscosity coefficients for air |
| $G_k$ | turbulent kinetic energy | $\mu_k$ | velocity of the kth term |
| $k$ | turbulent flow energy | $\vec{\mu}_k$ | average velocity of the term $k$ |
| $L$ | hollow projectile length | $\mu_m$ | kinetic viscosity coefficient |
| $\dot{m}_{pq}$ | mass transfer rate from phase q to phase p | $\mu_t$ | turbulent viscosity |
| $\dot{m}_{qp}$ | mass transfer rate from phase p to phase q | $\mu_w$ | kinetic viscosity coefficients for water |
| $P_0$ | ambient pressure | $\rho_a$ | densities of air |
| $P_c$ | water saturation vapor pressure. | $\rho_k$ | density of the phase $k$ |
| $R_B$ | gas nucleus radius | $\rho_m$ | mixture density |
| $S$ | source term | $\rho_q$ | density of phase q |
| $S_k$ | turbulent dissipation rate source term | $\rho_w$ | densities of water |
| $S_\varepsilon$ | turbulent energy term | $\sigma$ | cavitation number |
| $\alpha_k$ | volume fraction of the phase $k$ | $\tau_{ij}$ | shear stress |

in the distance between the two spheres during water entry.

The stability of different projectile entry water shapes (Akbari et al., 2020), cavitation characteristics (Luo et al., 2019), evolutionary characteristics of the cavity (Ma et al., 2014; Shi et al., 2019), and hydrodynamic properties (Hu et al., 2023) have been studied by numerous scholars in recent years. Wang et al. (2017) and Huang et al. (2018) conducted experimental studies on the low-velocity vertical water entry process of flat-tipped and 90° cone-tipped projectiles. The effects of cavity closure on the evolution of the water entry cavity and projectile motion characteristics were analyzed. Mu et al. (2019) conducted a numerical simulation of the oblique water entry of a high-speed rotating body. The evolution of the cavity shape, motion characteristics, and hydrodynamic properties at different water entry angles were analyzed. Hou et al. (2020) experimentally investigated the effect of the super cavity generated by a projectile at a small angle and high speed into the water on the ballistic trajectory of the projectile and the damage caused by the high load on the projectile body. Zhou and Shi (2022) investigated the problem of high-speed water entry in tandem revolved bodies and obtained the evolution law of the water entry cavities in the tandem revolved bodies under different water entry times. Liu et al. (2023) compared three head types—a cylindrical flat, hemispherical, and 90° tapered head—to analyze the effect of the head type on the stability of the projectile at high speed in water. In summary, research on spheres and different shapes of solid projectiles has been conducted for several years, and more research results have been obtained from both numerical simulations and experiments. However, not enough research has been conducted on hollow projectiles in water.

In recent years, some scholars have studied the aerodynamic and low-velocity water entry characteristics of hollow projectiles using numerical simulations and experiments. The study of aerodynamic properties focuses on the analysis of the wave system structure of its flow field (Qian et al., 2011), and the drag (Zhang et al., 2016) and blocking characteristics (Du et al., 2018; Quan et al., 2021) under different flight conditions. Further, some scholars have studied the shape of hollow projectiles for optimization using numerical simulations. Huang et al. (2013) conducted an exhaustive analysis of the different profiled 30 mm hollow projectiles using numerical simulation to obtain the profile parameter with the lowest drag coefficient. Zhao & Chen (2017) used a surrogate model combined with numerical simulations to optimize the hollow projectile shape and obtain the design parameters with the best drag reduction effect. Wessam et al. (2014) simulated the optimal hollow-projectile flow field for different Mach numbers and angles of attack and analyzed the effect of the angle of attack and Mach number on the drag and lift coefficients.

Savchenko (2011) investigated the hydrodynamic characteristics of a disc cavitator with a coaxial through-hole structure in a super cavitation flow. Hou et al. (2021) investigated the low-speed water entry of the hollow projectiles, thereby exploring the mechanism of the hollow cavity formation inside and outside the water, evolution characteristics of the jet, motion characteristics of the projectiles, and analyzing the influence law of the entry conditions. Jafari and Akbarzadeh (2022) experimentally investigated the water entry of hollow-cylinder projectiles with three holes. The results show different closure patterns with changes in the impact velocity and hole geometry. Liu et al. (2023)

experimentally investigated the oblique water entry of hollow cylinders with different internal diameters at low speeds. The multiphase flow characteristics of the cavities, through-hole jets, and multiscale cavities were revealed and discussed. In summary, current research on hollow projectiles mainly focuses on the aerodynamic aspects and low-speed vertical entry and oblique entry mechanisms of hollow projectiles of different shapes. However, the processes of the cavity evolution and cavitation characteristics of hollow projectiles with high speeds into water are less studied.

This study numerically calculated the high-speed vertical water entry process of hollow projectiles by using the VOF multiphase flow model, the Schnerr-Sauer cavitation model, and the overlapping mesh technique. The effects of the water entry velocity and through-hole diameter on cavity evolution, cavitation, and projectile motion characteristics, as well as the influence of frictional resistance on the motion of hollow projectiles, were analyzed in detail.

## 2. NUMERICAL METHODOLOGY

### 2.1 Flow Governing Equations

It is assumed that the water is incompressible during the entire process, while the heat dissipation owing to fluid viscosity is ignored in the water entry process. Considering the cavitation effect when entering the water at high speed, the gas, liquid, and vapor phases are set as phases 1, 2, and 3, respectively. The control equations of flow are expressed as follows:

(1) Continuity equations

$$\frac{\partial \rho_{\mathrm{m}}}{\partial \mathrm{t}}+\nabla\left(\rho_{\mathrm{m}} \vec{\mu}\right)=0 \tag{1}$$

where $\rho_{\mathrm{m}}$ is the mixture density and $\vec{\mu}$ is the average velocity of the mixture. Its expression is

$$\vec{\mu}=\frac{\sum_{\mathrm{k}=1}^{n} \alpha_k \rho_k \vec{\mu}_k}{\rho_m} \tag{2}$$

where $\alpha_k$, $\rho_k$, and $\vec{\mu}_k$ are the volume fraction of phase $k$, density of phase $k$, and velocity of term $k$, respectively.

(2) Momentum equation

$$\frac{\partial\left(\rho_{\mathrm{m}} \vec{\mu}\right)}{\partial \mathrm{t}}+\nabla \cdot\left(\rho_m \vec{\mu} \vec{\mu}\right)=-\nabla P+\nabla \tau_{ij}+S \tag{3}$$

where $P$ is the pressure, $S$ is the source term, and $\tau_{ij}$ is the shear stress, whose specific expression is

$$\tau_{ij}=\mu\left[\left(\frac{\partial \mu_i}{\partial x_j}+\frac{\partial u_j}{\partial x_i}\right)-\frac{2}{3} \delta_{ij} \frac{\partial \mu_k}{\partial x_k}\right] \tag{4}$$

where $\mu$ is the viscosity of the mixture and is expressed as $\mu=\sum_{k=1}^{n} \alpha_k \mu_k \mu_k$, where $\mu_k$ is the velocity of the kth term.

(3) Phase volume fraction

For phase q, the volume fraction equation can be expressed as

$$\frac{1}{\rho_q}\left[\frac{\partial}{\partial t}\left(\alpha_q \rho_q\right)+\nabla \cdot\left(\alpha_q \rho_q \vec{v}_q\right)\right]=\mathrm{S}_{\alpha_q}+\sum_{\mathrm{p}=1}^{\mathrm{n}}\left(\dot{\mathrm{m}}_{\mathrm{pq}}-\dot{\mathrm{m}}_{\mathrm{qp}}\right) \tag{5}$$

where $\rho_q$ is the density of phase q, $\alpha_q$ is the volume fraction of phase q, $\dot{\mathrm{m}}_{\mathrm{pq}}$ is the mass transfer rate from phase q to phase p, and $\dot{\mathrm{m}}_{\mathrm{qp}}$ is the mass transfer rate from phase p to phase q.

(4) Volume fraction conservation equation

$$\sum_{q=1}^{n} \alpha_q=1 \tag{6}$$

### 2.2 Volume of Fluid Multiphase Flow Model

The volume-of-fluid multiphase flow model treats the multiphase fluid as a mixed-fluid medium of variable density. The volume fraction of each phase of the fluid medium in each control cell within the fluid calculation domain was solved to determine the components of each phase of the fluid within that cell, thus enabling the capture of the interface between the phases of the fluid. Assuming a liquid phase volume fraction of $\alpha_w$, $\alpha_w = 1$ in cells with a pure liquid phase and $\alpha_w = 0$ in cells with a pure gas phase, $0 < \alpha_w < 1$ at the gas-liquid interface.

The density $\rho_m$, kinetic viscosity coefficient $\mu_m$, and energy $E_m$ of this mixed medium are expressed as

$$\rho_m=\left(1-\alpha_w\right) \rho_a+\alpha_w \rho_w \tag{7}$$

where $\rho_a$ and $\rho_w$ are the densities of air and water, respectively.

$$\mu_m=\left(1-\alpha_w\right) \mu_a+\alpha_w \mu_w \tag{8}$$

where $\mu_a$ and $\mu_w$ are the kinetic viscosity coefficients for air and water, respectively.

$$E_m=\frac{\left(1-\alpha_w\right) \rho_a E_a+\alpha_w \rho_w E_w}{\rho_m} \tag{9}$$

where $E_a$ and $E_w$ are the total energies of air and water, respectively.

### 2.3 Realizable *k-ε* Turbulence Model

The realizable *k-ε* model is a modification of the standard *k-ε* model.

The *k-ε* turbulence model is a two-equation model for solving turbulent viscosity $\mu_t$. The solutions to the transport equation for turbulent flow energy $k$ and transport equation for turbulent dissipation rate $\varepsilon$. In this study, the realizable *k-ε* turbulence model was used, where turbulent viscosity $\mu_t$ is expressed as

$$\mu_t=\rho_m C_\mu \frac{k^2}{\varepsilon} \tag{10}$$

where $\varepsilon$ is the turbulent dissipation rate, expressed as $\varepsilon = \frac{\mu}{\rho}\overline{\left(\frac{\partial u_i'}{\partial x_k}\right)\left(\frac{\partial u_i'}{\partial x_k}\right)}$, and $C_\mu$ is an empirical constant.

$k$ and ε equations are as follows:

$$\frac{\partial(\rho_m k)}{\partial t}+\frac{\partial(\rho_m k u_i)}{\partial x_i}=\frac{\partial}{\partial x_i}\left[\left(\mu+\frac{\mu_t}{\sigma_k}\right)\frac{\partial k}{\partial x_i}\right] \quad (11)$$
$$+G_k+G_b-\rho_m\varepsilon-Y_M+S_k$$

$$\frac{\partial(\rho_m \varepsilon)}{\partial t}+\frac{\partial(\rho_m \varepsilon u_i)}{\partial x_i}=\frac{\partial}{\partial x_i}\left[\left(\mu+\frac{\mu_t}{\sigma_\varepsilon}\right)\frac{\partial \varepsilon}{\partial x_i}\right] \quad (12)$$
$$+\rho_m C_1 S\varepsilon-\rho_m C_2\frac{\varepsilon^2}{k+\sqrt{v\varepsilon}}+C_{1\varepsilon}\frac{\varepsilon}{k}C_{3\varepsilon}G_b+S_\varepsilon$$

where $G_k$ is the turbulent kinetic energy induced by the velocity gradient. $G_k=\mu_t S^2$; $G_b=\beta g_i\frac{\mu_t}{Pr_t}\frac{\partial T}{\partial x_i}$ is the turbulent energy caused by buoyancy (of which $\beta=-\frac{1}{\rho}\left(\frac{\partial \rho}{\partial T}\right)_P$, $Pr_t$=0.85); $Y_M=2\frac{\rho k\varepsilon}{\gamma RT}$; $C_1=\max[0.43,\frac{\eta}{\eta+5}]$; $\eta=\frac{Sk}{\varepsilon}$; $S=\sqrt{2S_{ij}S_{ij}}$; $S_{ij}=\frac{1}{2}\left(\frac{\partial u_i}{\partial x_j}+\frac{\partial u_j}{\partial x_i}\right)$; and $C_{1\varepsilon}$=1.44; $C_2$=1.9; $\sigma_k$=1.0; $\sigma_\varepsilon$=1.2. $S_\varepsilon$ and $S_k$ are the turbulent energy term and dissipation rate source term, respectively.

### 2.4 Schnerr-Sauer Cavitation Model

According to Bernoulli's equation, the pressure decreases with an increase in the flow rate of water. When the pressure decreases to the saturated vapor pressure, the water vaporizes. The cavitation number $\sigma$ is an important relationship that expresses the degree of cavitation and is expressed as

$$\sigma=\frac{p_0-p_c}{\frac{1}{2}\rho v^2} \quad (13)$$

where $p_0$ and $p_c$ are the ambient pressure and the water saturation vapor pressure of the current corresponding temperature, respectively.

The Schnerr-Sauer model, based on the Rayleigh-Plesset air bubble equation, was used to solve the cavitation phenomenon in this study.

The mass transport equation for the vapor phase is

$$\frac{\partial \alpha_v}{\partial t}+\frac{\partial}{\partial x_i}(\alpha_v u_i)=F_{vap}\frac{2\alpha_{nuc}(1-\alpha_v)\rho_v}{R_B} \quad (14)$$
$$\sqrt{\frac{2}{3}\frac{p_v-p}{\rho_l}}-F_{cond}\frac{3\alpha_v\rho_v}{R_B}\sqrt{\frac{2}{3}\frac{p-p_v}{\rho_l}}$$

where the gas nucleus radius $R_B=1\times10^{-6}$, the volume fraction of the non-condensable gas $\alpha_{nuc}=5\times10^{-4}$, and

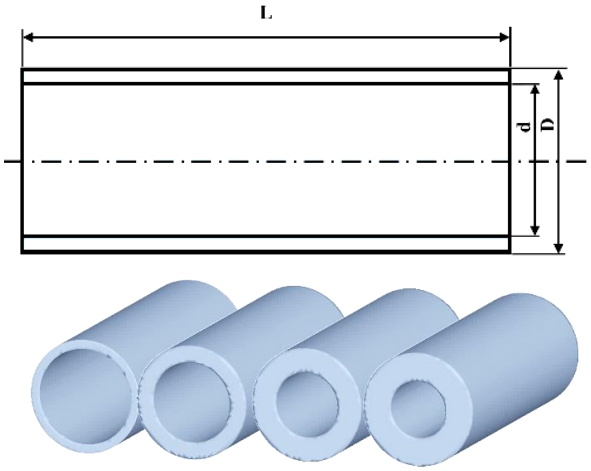


**Fig. 1 Calculation Model**

**Table 1 Parameters of the numerical model**

| Serial number | $D$/mm | $d$/mm | $L$/mm | $m$/kg | $d/D$ |
|---|---|---|---|---|---|
| M1 | 30.0 | 25.3 | 80.0 | 0.128 | 0.83 |
| M2 | 30.0 | 21.3 | 80.0 | 0.220 | 0.71 |
| M3 | 30.0 | 17.3 | 80.0 | 0.296 | 0.58 |
| M4 | 30.0 | 15.3 | 80.0 | 0.444 | 0.51 |

the empirical constant $F_{vap}=50$ and $F_{cond}=0.001$.

### 2.5 Computational Model

This study investigated the hollow projectile model shown in Fig. 1. The four models had the same outer diameter and length (outer diameter $D$ = 30 mm and length $L$ = 80 mm). The material was 45-gauge steel, and the center of mass was 40 mm from the head of the model. The inner diameter $d$ and mass m of the four models were not consistent. The specific parameters are presented in Table 1.

This study used the VOF fluid domain volume model to capture the variation in the free liquid level. The solution is based on the Schnerr-Sauer model derived from the Rayleigh-Plesset bubble equation. The overlapping mesh technique and DFBI motion model were used to capture the motion of the projectile.

The grid of the $x$=0 symmetric section is shown in Fig. 2. Linear interpolation was used to exchange data between the overlapping and background grid. To capture

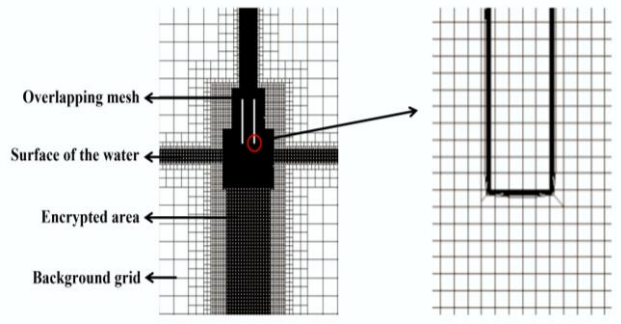


**Fig. 2 Partial grid of $x$=0 symmetric section**

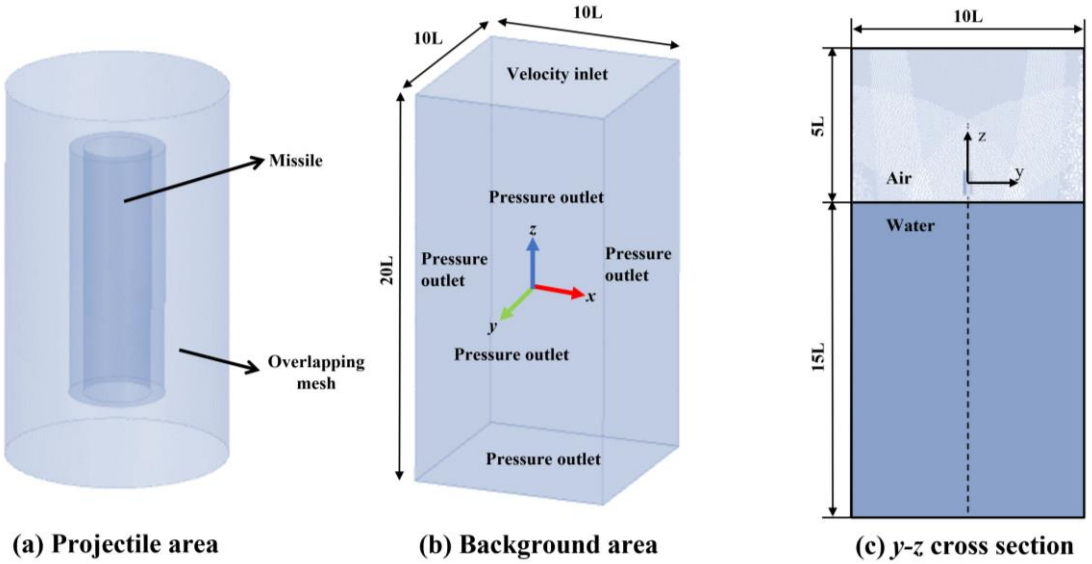


**Fig. 3 Calculation domain and boundary condition setting**

**Table 2 Calculation of working parameters**

| Working conditions | Model | Velocity (m/s) | Time step (s) |
|---|---|---|---|
| Case 1 | M1 | 50 | $1\times10^{-5}$ |
| Case 2 | M1 | 100 | $5\times10^{-6}$ |
| Case 3 | M1 | 150 | $4\times10^{-6}$ |
| Case 4 | M1 | 200 | $3\times10^{-6}$ |
| Case 5 | M2 | 100 | $5\times10^{-6}$ |
| Case 6 | M3 | 100 | $5\times10^{-6}$ |
| Case 7 | M4 | 100 | $5\times10^{-6}$ |

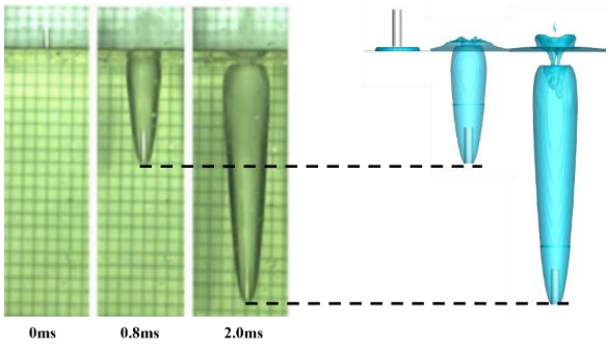


**Fig. 4 Comparison between the experimental and numerical calculation of water entry cavity**

the flow field changes during projectile motion more precisely, the projectile perimeter and motion trajectory were encrypted. The calculation domain condition settings are shown in Fig. 3. The length and width were 10 L, the water depth was 15 L, and the air area was 5 L. The top, round, and bottom areas of the calculation domain were set as the velocity inlet and pressure outlet, respectively. The second-order implicit form was used to discretize the time, and the specific working conditions are presented in Table 2.

### 2.6 Numerical Method Validation

To verify the accuracy of the numerical simulation method for calculating the high-speed water entry process of hollow projectiles in this study, the experimental results in Chen et al. (2019) were selected as a control. In this validation model, a cylinder with a diameter, length, mass, and initial velocity of 6 mm, 24 mm, 4.88 g, and 106.7 m/s, respectively, was used. The evolution process of the water entering the cavity obtained by numerical calculation was compared to the experiment in the literature. As shown in Fig. 4, both underwent the processes of water impact, open cavity, cavity stretching, expansion stage, and surface closure. The size of the cavity and depth of the projectile are essentially similar to those in the experiment at the same time, which verifies the accuracy of the present numerical calculation model in terms of cavities.

A comparison of the numerical simulation and experimental results of the velocity and displacement curves is shown in Fig. 5. The velocity and displacement of the projectile decay and increase with time, and the maximum error of the velocity between the numerical simulation and experimental results is approximately 6.7%. Here, the maximum error of the displacement is approximately 3.4%. The errors of the obtained velocity and displacement curves are within acceptable limits when compared to the experimental results, which also verifies the correctness of the present numerical calculation model in terms of the motion characteristics of the cylinder.

## 3. Results And Discussion

### 3.1 Effect of Water Entry Speed

#### 3.1.1 Analysis of Water Entry Cavities Morphology

The four working conditions, 1–4, were calculated using numerical simulation to analyze the mechanism of cavity evolution in the same aperture with four different velocities entering the water.

The evolution of the cavity, when the hollow projectile entered the water at 50 m/s, is shown in Fig. 6. The moment of projectile contact with the water surface

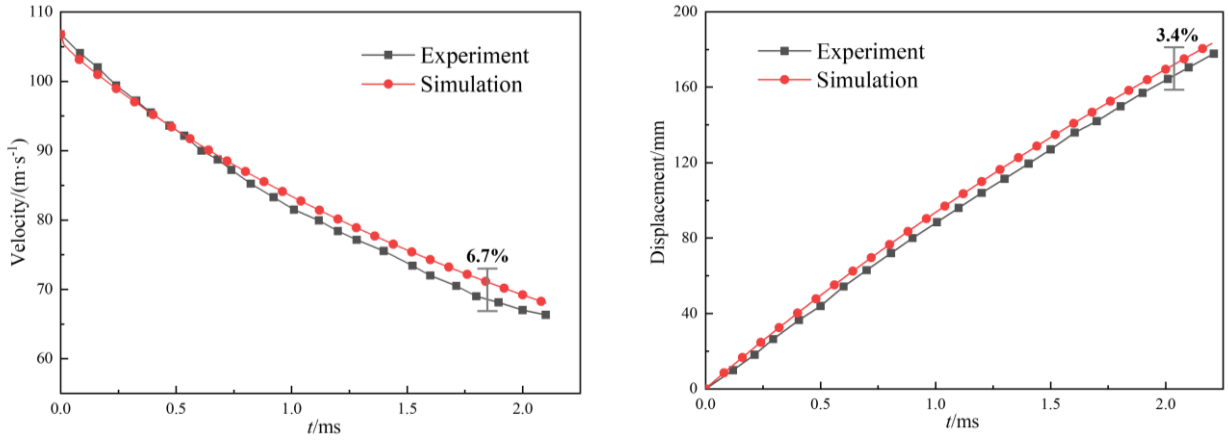


(a) Velocity curves (b) Displacement curves

**Fig. 5 Velocity and displacement curves with time**

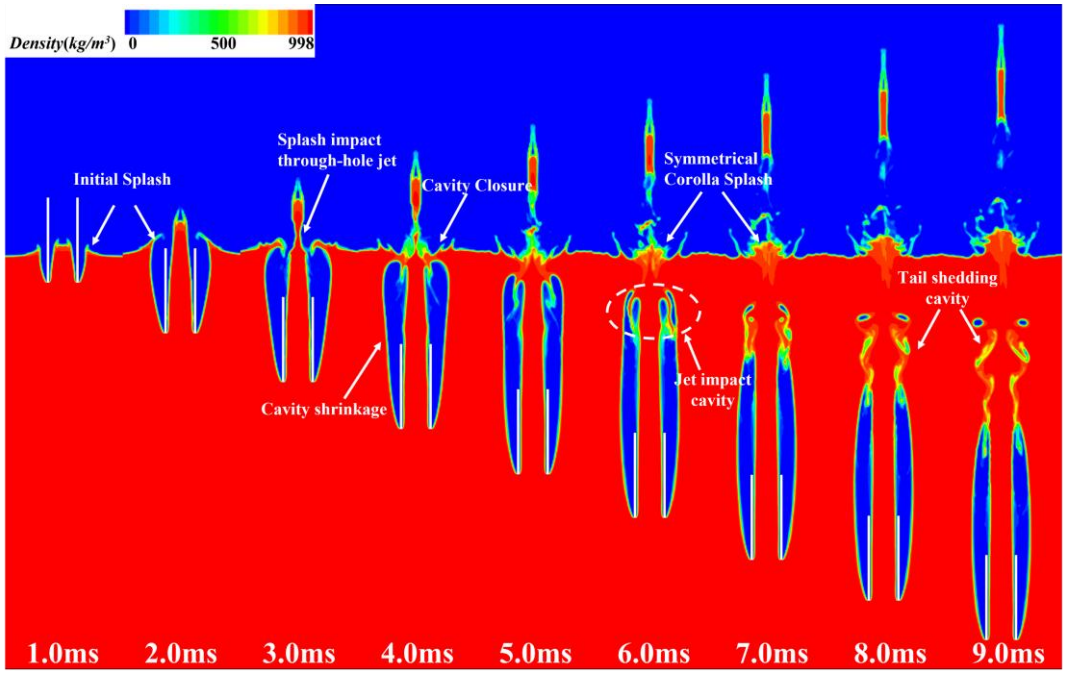


(a) Water volume fraction of the *x-z* section

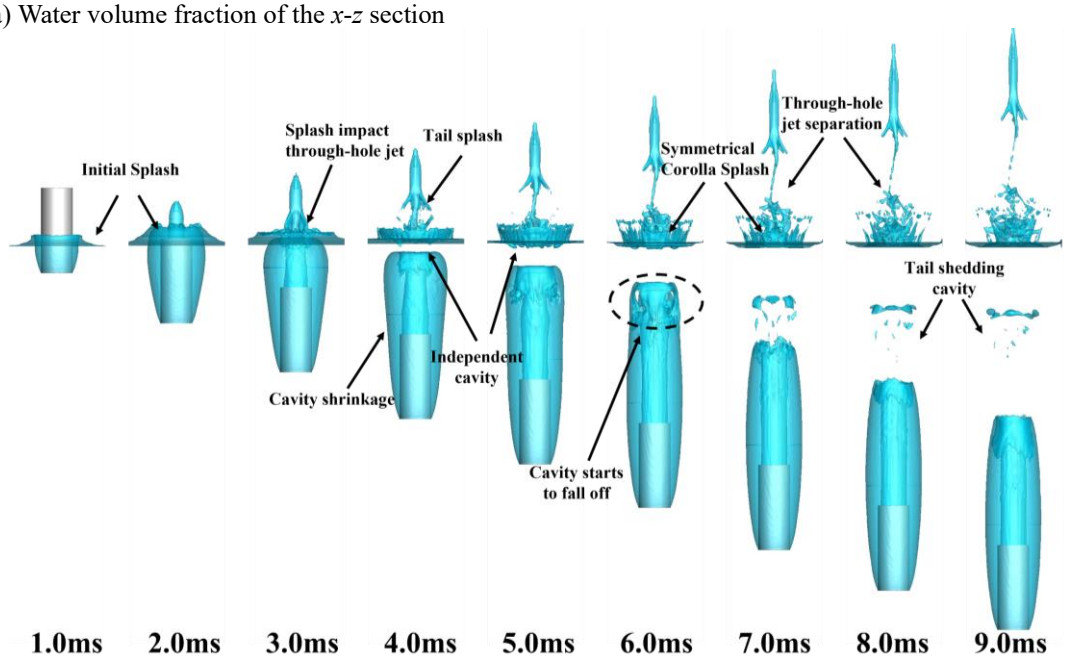


(b) Cavity shape evolution by the air-liquid equivalence surface

**Fig. 6 Water volume fraction of the *x-z* section and cavity shape evolution at 50 m/s**

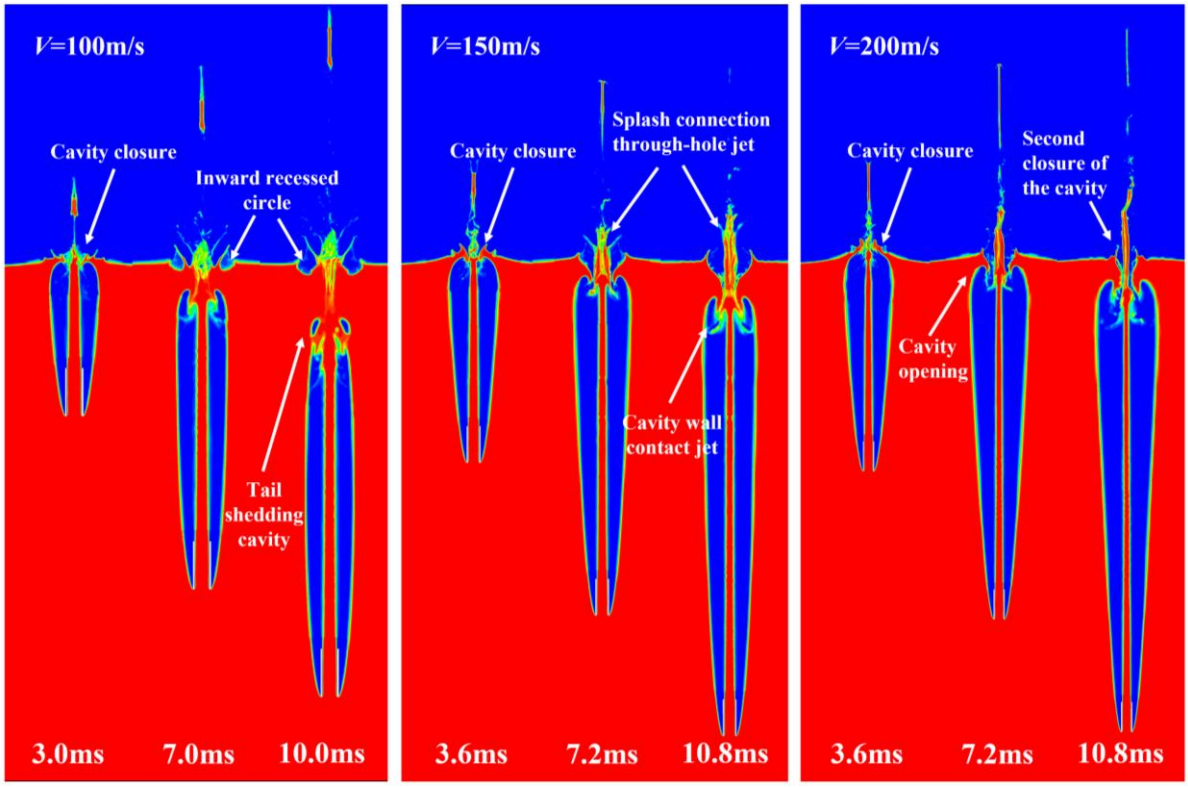


**Fig. 7 Water volume fraction of the *x*-*z* section at 100–200 m/s**

was taken as the 0 ms moment. The evolution of the cavity is roughly divided into four stages: impact on the water surface, cavity stretching, cavity contraction closing, and cavity contraction collapse. At $t$=1 ms, the hollow projectile head hits the water surface, thereby causing water to be squeezed to gain kinetic energy and move to the inner and outer sides. The fluid moving inward was restrained by the through-hole, thus causing it to flow upward. This is known as the through-hole jet. Here, a splash is generated by an outwardly flowing liquid.

The cavity gradually expanded at 3 ms. Owing to the atmospheric pressure, the splash generated an inward velocity that caused the splash to impact the through-hole jet. The kinetic energy of the splash was transferred to the through-hole jet, thereby generating upward and downward velocities.

The cavity was completely closed at 4 ms, while the splash was completely in contact with the through-hole jet. Under the pressure of water, the cavity starts to contract from the middle and moves toward the tail of the cavity. Under the impact of the splash, the through-hole jet produced an arrow-shaped splash that moved upward. At $t$=6 ms, the walls of the shrinking cavity collide with the downward splash generated when the cavity closes, the cavity begins to fall off, and the splash is a symmetrical corolla. Between 7–9 ms, the shedding of the small cavity gradually increased under the pressure of the surrounding water.

The evolution of the cavity, when the hollow projectile entered the water at 100–200 m/s, is shown in Fig. 7. The evolution of the cavity was roughly divided into four stages: impact on the water surface, cavity stretching, cavity stretching closing, and cavity contraction. The cavity closure occurs at 3 ms ($V$=100 m/s) and 3.6 ms ($V$=150, 200 m/s). The higher the velocity, the larger the cavity and the further the cavity closes. At 7 ms ($V$=100 m/s), the free surface produced an inwardly recessed circle. This is because the surrounding splash impacts the through-hole jet and later moves outward with an oblique upward velocity. At 7.2 ms ($V$=150 m/s), the thinner splash continues to move toward the through-hole jet under atmospheric pressure, connecting the through-hole jet and producing an inwardly recessed circle. At 7.2 ms ($V$=200 m/s), the thinner splash separates from the thicker splash, and the cavity is converted from closed to incompletely closed. At 10 ms ($V$=100 m/s), the inwardly recessed circle moved upward, thereby causing the cavity tail to shed. At 10.8 ms ($V$=150 m/s), the downward moving splash contacts the cavity wall, thereby causing the cavity to enter the shedding stage. At 10.8 ms ($V$=200 m/s), the cavity completes its secondary closure.

The diameter of the cavity at 50 mm below the free surface is shown in Fig. 8. The hollow projectile entering the water at 50 m/s has a maximum cavity diameter of approximately 54.2 mm at 6.4 ms. At an initial velocity of 100 m/s, the cavity diameter reaches its maximum at 6.5 ms, approximately 84.7 mm. At an initial velocity of 150 m/s, the cavity diameter reaches its maximum at 8.4 ms, approximately 120.1 mm. At an initial velocity of 200 m/s, the cavity diameter reaches its maximum at 10.2 ms, approximately 159.4 mm. The time required for the cavity to reach its maximum diameter increased as the speed increased. As shown in Fig. 8, the contraction speed of the cavity was faster than the expansion speed. This is owing to the fact that as the depth of the projectile in the water increases, the velocity decreases, the pressure of the water outside the cavity increases, and the cavity shrinks faster.

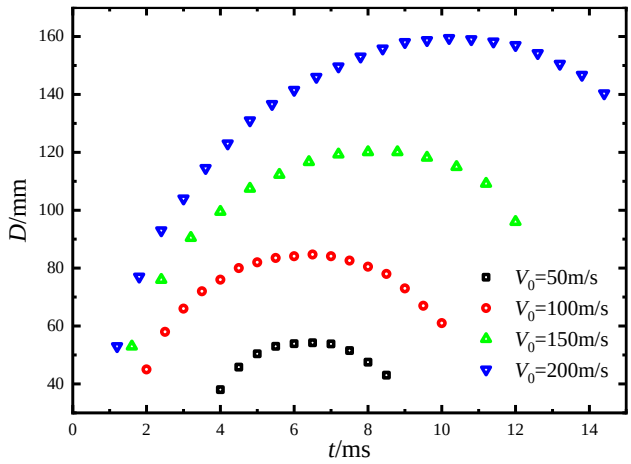


**Fig. 8 Diagram of the cavity diameter at 50 mm below the free surface**

### 3.1.2 Analysis of Cavitation Characteristics of Water Entry

The volume fraction of the vapor phase for the water entry at four different velocities is shown in Fig. 9. The cavitation phenomenon became more pronounced as the initial velocity of the water entry increased.

At $V$=50 m/s, vapor was observed at 3 ms at the end of the outer wall surface of the cavity and through-hole jet. Here, the vapor starts to appear on the wall of the outer cavity at 4 ms and is more pronounced at the end of the through-hole jet. The vapor in the tail of the outer cavity wall surface gradually disappeared at 5 ms, and the vapor at the end of the through-hole jet was divided into two sections and gradually moved upward. At 6 ms, the vapor on the outer wall of the cavity became more obvious and was generated toward the center of the cavity. Here, the vapor in the tail disappears completely, and the vapor phase in the tail of the through-hole jet changes from two sections to one section. Further, the vapor on the outer wall surface of the cavity became more obvious at 7 ms, and the vapor at the end of the through-hole jet became dislodged from the cavity and gradually disappeared. As shown in Fig. 10, the air and vapor wetting diagram of the projectile surface and the entire process of the outer wall surface of the projectile were mainly enveloped by air. The inner wall of the projectile had more air at 3 ms. However, after 3 ms, the vapor gradually increased, and at 7 ms, it was mainly air, vapor, and water.

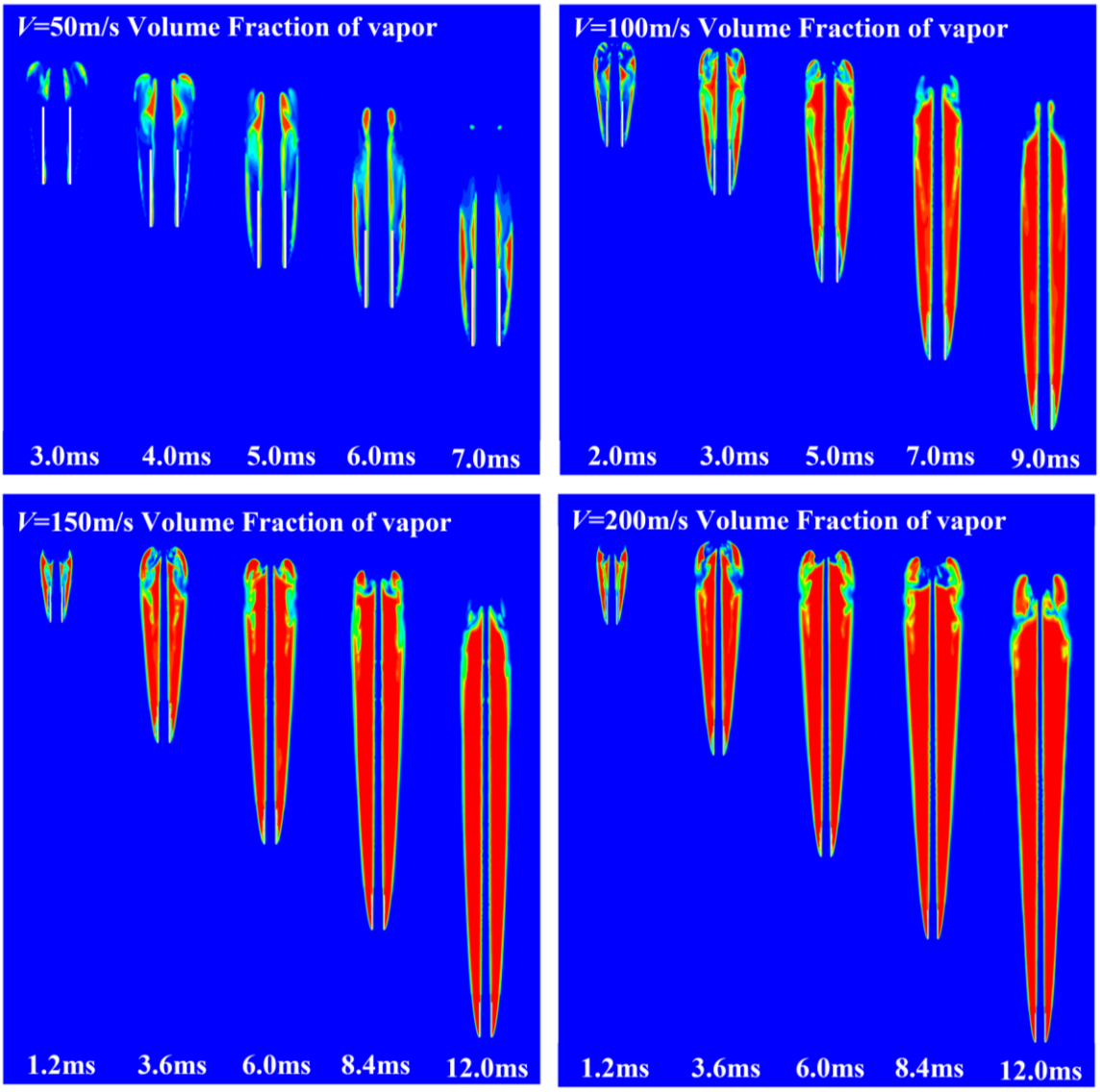


**Fig. 9 Vapor volume fraction at 50–200 m/s**

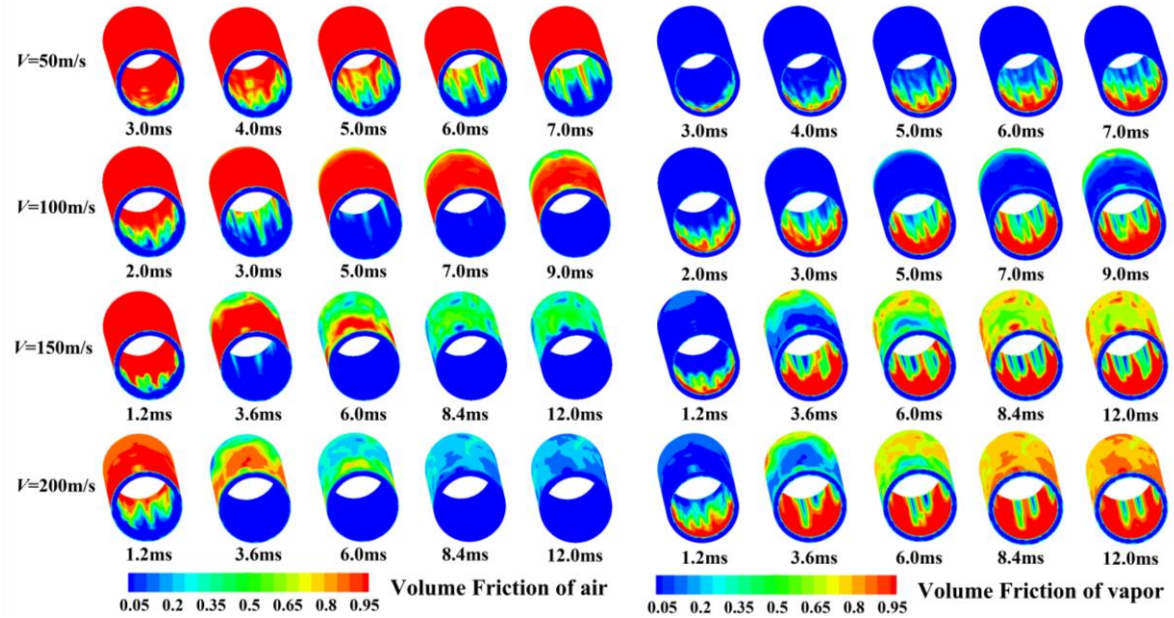


**Fig. 10 Wetting diagram of the air and vapor at 50–200 m/s**

When *V*=100 m/s, the vapor on the outer wall surface of the cavity was generated inward at 3 ms, and that on the through-hole jet was generated outward. Both vapors are connected at 5 ms. Furthermore, the volume of the vapor increases with an increase in the depth of the water entry. The vapor at the end of the outer cavity gradually fades into the cavity at 7 ms. Here, the entire vapor distribution is relatively stable, uniform, and symmetrical at 9 ms. However, the cavity shrinks, thereby resulting in a decrease in the tail vapor. As shown in Fig. 10, before 5 ms, the outer wall surface of the projectile was wrapped mainly with air, but after 5 ms, the vapor started appearing in the tail of the projectile. Before 5 ms, the air and vapor flowed through the inner wall of the projectile, although the main component was air. With the time delay, the percentage of the vapor gradually increased, and after 5 ms, the inner wall of the projectile was mainly vapor.

When the initial velocities are 150 and 200 m/s, the volume increases with increasing speed. The vapor with an initial velocity of 150 m/s started to contract steadily at 12 ms, but the vapor with an initial velocity of 200 m/s continued to expand. As shown in Fig. 10, before 1.2 ms, the outer and inner wall surfaces of the projectile are mainly made of air. As the depth of the water entry increased, the amount of the vapor on the outer wall surface increased rapidly and covered the entire surface. There was almost no air on the inner wall surface, and the vapor filled almost the entire inner wall surface. The percentage of air and vapor on the inner and outer surfaces of the projectile is similar at 8.4 ms. Hence, the frictional resistance is similar, as shown in Fig. 12.

### 3.1.3 Analysis of the Hydrodynamics and Motion Characteristics of the Projectile

Figure 11 shows the evolution of the projectile motion parameters and drag coefficients with time for four different velocities. The curves of velocity, displacement, acceleration, and drag coefficient with time for hollow projectiles at different velocities are shown. As shown in Fig. 11(a–c), the effect of gravitational acceleration on the projectile after entering water is not considerable owing to the high velocity. The lower the entry velocity, the smaller the change in the velocity. As the depth of water entry increased, the displacement growth reduced. When entering water, the projectile is converted from the fluid medium of less dense air to more dense water, thereby resulting in greater resistance. Here, the acceleration produced a peak. The peak value of drag acceleration increases as the water entry velocity increases and stabilizes after entering the water. When entering water, the acceleration at higher velocities is always greater than that at lower velocities. As shown in Fig. 11(d), the drag coefficient of the projectile peaks when it enters the water and then stabilizes. The drag coefficient of the projectile with an entry velocity of 50 m/s is greater than that of the other three velocities.

Figure 12 shows the variation in the frictional resistance of the hollow projectile M1 when it enters water at different velocities. Let the resistance in the downward direction be positive and that in the upward direction be negative. As shown in Fig. 12, when the initial velocity is 50 m/s, the frictional resistance is small and is approximately 0. As shown in Fig. 10, this is owing to the lower speed. Here, the outer surface of the projectile is basically entirely air, while most of the inner surface comprises vapor and air. As such, there is less water on the wall surface of the projectile, thereby resulting in a reduced frictional resistance. With different velocities in the water, the frictional resistance first increased and later decreased. Hence, the greater the velocity, the greater the frictional resistance, and the earlier the frictional resistance reaches its peak value. As shown in Fig. 12(a), the frictional resistance reaches its maximum value when the surface of the projectile is stained with the majority of the water. The greater the velocity, the more water on the outer wall surface of the projectile, and the greater the frictional resistance generated. When entering the water at an initial velocity of 150–200 m/s, the frictional resistance

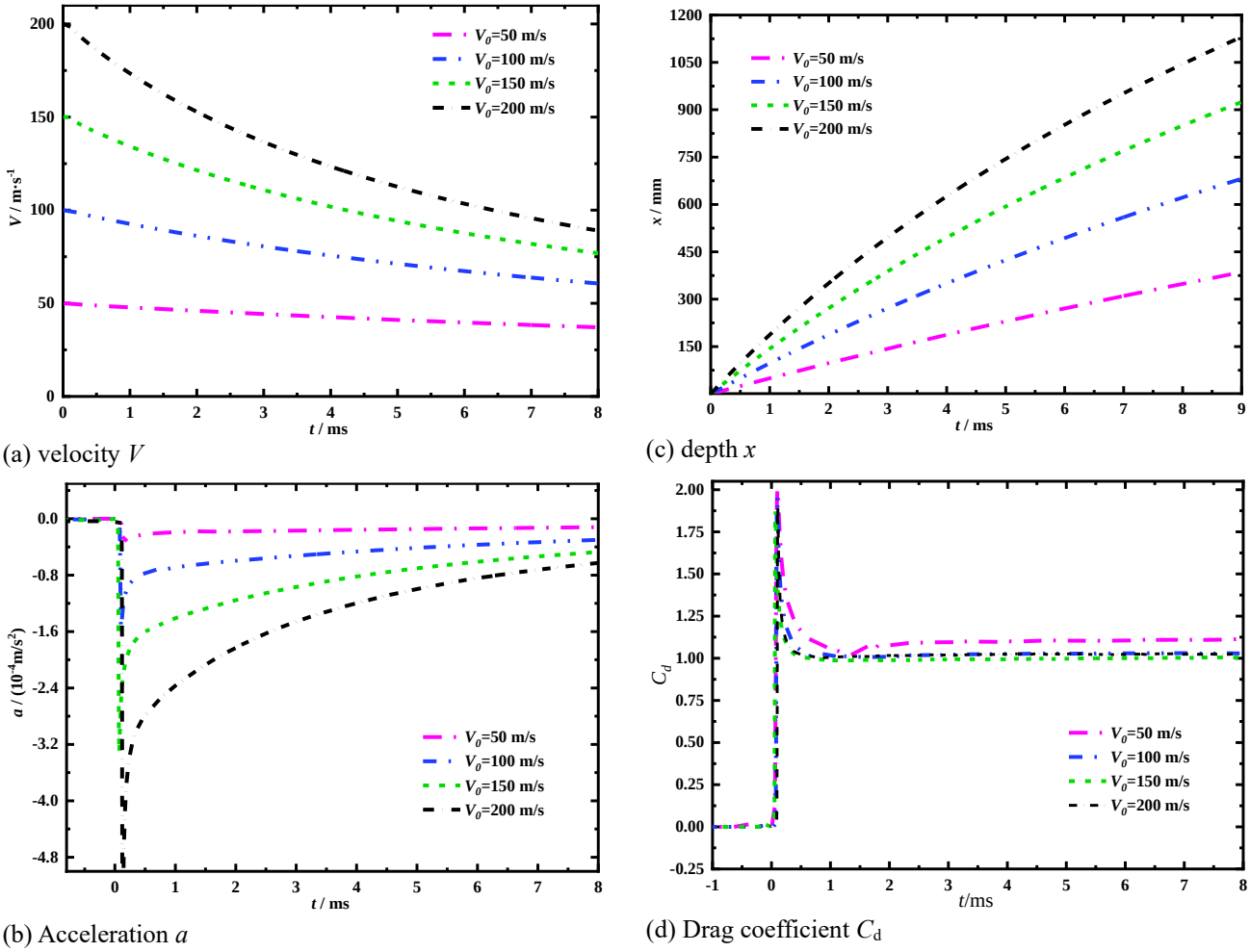


(a) velocity $V$ (c) depth $x$

(b) Acceleration $a$ (d) Drag coefficient $C_d$

**Fig. 11 Variation of motion parameters and drag coefficient with time for hollow projectiles with different velocities**

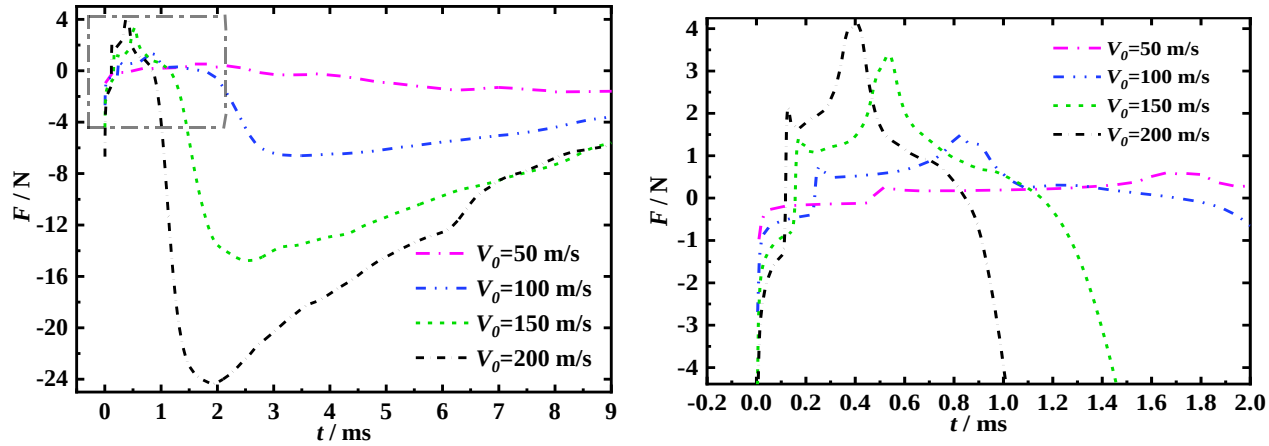


(a) Variation of frictional resistance from 0–9 ms (b) Variation of frictional resistance from 0–2 ms

**Fig. 12 Variation of frictional resistance at different velocities of hollow projectile M1**

is similar after 8 ms. This is owing to the insignificant difference in the amount of gas, vapor, and water wetting the surface of the projectile at higher velocities after the projectile has been completely stabilized in the water.

As shown in Fig. 12(b), the frictional resistance of the hollow projectile increases to a maximum and later decreases before the hollow projectile is completely in water. When the hollow projectile hits the water surface at a high velocity, the external gas flows rapidly toward the wall of the projectile, thereby generating a velocity faster than the motion of the projectile. This projectile is subject to a downward frictional resistance generated by the gas on the wall. As such, the frictional resistance first rises to a positive number. Further, there were two-step points before the hollow projectile that completely entered the water. The first step point is reached when the head of the hollow projectile impacts the water surface, the inner or outer wall surface of the hollow projectile is rapidly

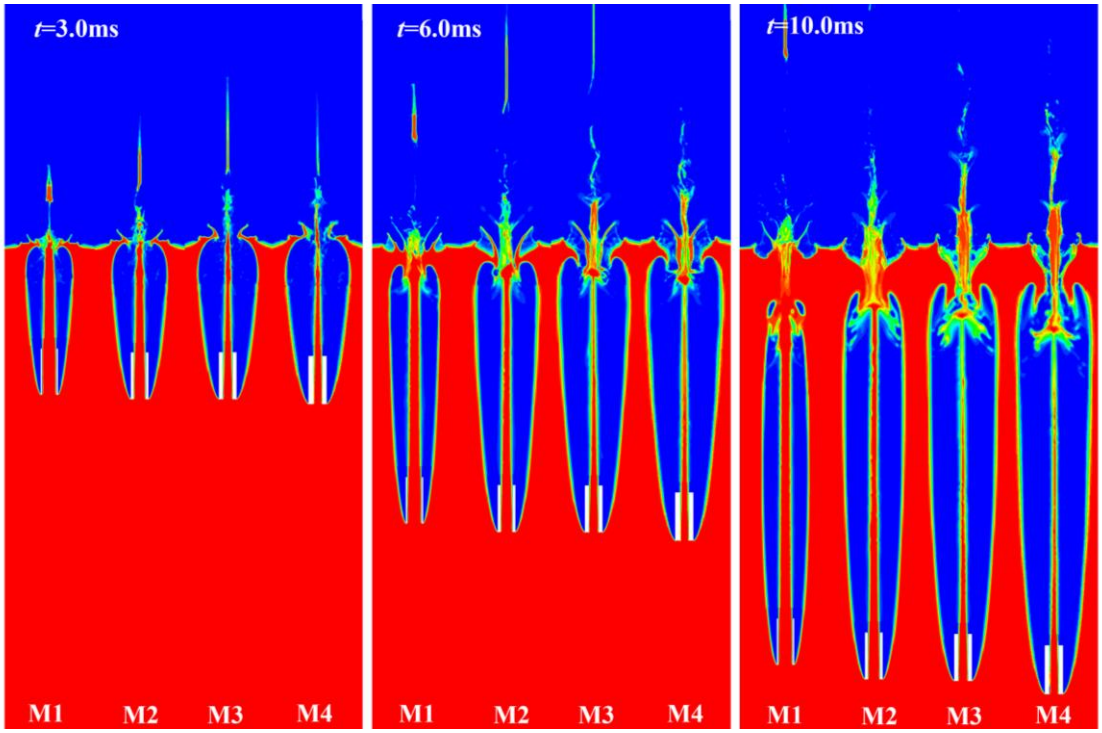


**Fig. 13 Partial evolution of the cavity when M1–M4 enters the water at 100 m/s**

wetted, and the frictional resistance of the projectile body changes from only gas to water and gas acting together, producing the first step point. The second step point is when the hollow projectile is completely in water, and the vapor on the inner wall surface of the hollow projectile produces more frictional resistance. At this point, the frictional resistance generated by vapor and water and the frictional resistance generated by only air cancel each other, thereby causing the frictional resistance to reach its maximum value. As shown in Fig. 12, the higher the initial velocity of the water entry, the earlier the step point is generated.

### 3.2 Effect of Through-Hole Diameter

#### 3.2.1 Analysis of Water Entry Cavity Morphology

The high-speed water entry of four types of hollow projectiles was investigated using numerical simulations, and the cavity evolution mechanism of different apertures at the same entry velocity was analyzed.

Fig. 13 shows the partial evolution of the cavity when M1–M4 impacted the water surface at 100 m/s. The aperture ratio ($d/D$) of M1-M4 is presented in Table 1. Before $t$=3 ms, the hollow projectile undergoes the stage of opening the cavity by impacting the water surface. The cavity diameters of M1–M4 at 3 ms were considerably different. The smaller the inner diameter of the hollow projectile, the larger the cavity after entering the water. This is because for a similar outer diameter of the hollow projectile, the smaller the inner diameter, the greater the mass of the hollow projectile and contact area with the water surface, and the more kinetic energy is generated at the same speed and transferred to the splash. At 3 ms, the phenomena of M1 and M2 surface closure and secondary splash formation in all directions began. Here, the M3 and M4 surfaces were not yet close. As such, the thinner splash collides with the through-hole jet, which later separates. Further, the through-hole jet reacts to the splash, thereby causing the splash to expand outward and impeding the cavity from closing. The smaller the inner diameter of the hollow projectile, the greater the kinetic energy of the through-hole jet and the longer the distance it travels simultaneously.

At $t$=6 ms, the cavity diameter of M1 was the smallest, while that of M4 was the largest. The cavity created by M1 was completely independent of the water surface. Here, the splash of M2 strikes the through-hole jet to produce an outwardly directed annular jet, which clings to the outer wall surface of the jet. The annular jets generated by M3 and M4 were separated from the cavity, and the cavity was converted from closed to unclosed. At $t$=10 ms, the cavity of M1 gradually shrinks, while the trailing cavity starts falling off. The cavities created by M2, M3, and M4 formed a downward depressed circle at the water surface, which was formed by the impact connection between the splash and the through-hole jet. Part of the kinetic energy was transferred upward to form a depressed circle, while it was transferred downward to form a splash jet inside the cavity.

The diameter of the cavity at 50 mm below the free surface is shown in Fig. 14. The smaller the inner diameter of the hollow projectile, the higher the amount of kinetic energy transferred to the water, and the larger the diameter of the cavity. In the cavity expansion phase, the smaller the inner diameter, the faster the cavity expansion. However, the time to reach the maximum diameter is basically similar. The maximum diameter reached by the cavity formed by the M1, M2, M3, and M4 projectiles were approximately 85.1 mm, 105.5 mm, 115.4 mm, and 119.8 mm, respectively. When the inner diameter was larger, the surface area increased by reducing the same

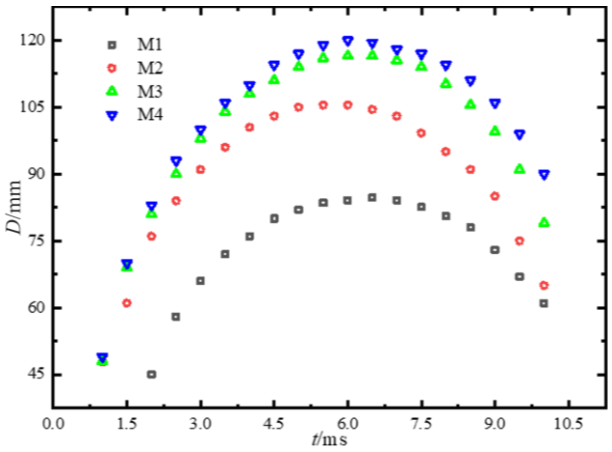


**Fig. 14 Diagram of the cavity diameter at 50 mm below the free surface (*V*=100 m/s)**

inner diameter. Hence, as the inner diameter decreases, the maximum diameter of the cavity increases less considerably. In the cavity contraction stage, the smaller the inner diameter of the hollow projectile, the more evident and faster the cavity contraction and contraction rate. This is owing to the fact that the smaller the inner diameter of the hollow projectile, the larger the diameter of the cavity produced, and the greater the pressure on the cavity from outside the cavity.

### 3.2.2 Analysis of Cavitation Characteristics of the Cavity

The evolution of cavitation when the four hollow projectiles enter water with an initial velocity of 100 m/s is shown in Fig. 15. At *t*=2 ms, the cavitation of all four aperture projectiles starts from the cavity wall surface and through-hole jet wall surface. The smaller the inner diameter of the projectile, the more obvious the cavitation at *t*=2 ms and the larger the cavitation area. As shown in Fig. 16, at *t* =2 ms, the outer surfaces of the different inner diameters of the projectile are almost entirely air, while the inner surface of the projectile is a mixture of air and vapor. The vapor is generated near the head of the hollow projectile toward the tail owing to the high velocity of the water flow in the head. Here, the vapor adheres to the inner wall surface of the hollow projectile.

As shown in Fig. 15, at *t*=5 ms, the vapor moves backward from the head of the cavity along the through-hole, thereby resulting in the cavitation expansion from the wall surface of the cavity to the inside of the cavity. When the hollow projectiles are M1 and M2, the cavitation phenomenon fills almost the entire cavity. In the case of hollow projectiles such as M3 and M4, there is a part of the cavity that is not cavitated in the middle part of the cavity. This is because at *t*=5 ms, the cavity created by M3 and M4 is not completely closed, and there is more air in the cavity. As shown in Fig. 16, the outer surface of the four apertures of the projectile at *t*=5 ms is a mixture of air and vapor, wherein air still occupies the major component. This is because cavitation starts being generated inward from the outer wall surface of the cavity, and the vapor has not yet reached the outer wall surface of the projectile.

As shown in Fig. 15, at *t*=9 ms, the cavitation of the tail of the cavity with the M1 aperture of the projectile disappeared, and a more complete cavitation circle with a small tail was formed. When the aperture of the projectile is M2, most of the tail cavity is a mixture of vapor and air. When the projectile aperture was M3 or M4, there was a vapor ring at the end of the cavity, and cavitation was not evident in the small part of the middle of the cavity. As shown in Fig. 16, at *t*=9 ms, there was almost no air on the inner surface of the four aperture projectiles, with vapor and water near the head and tail, respectively. With the movement of the projectile, the vapor moved from the head to the tail. The smaller the inner diameter, the less vapor and the more water on the wall of the projectile body. The outer wall surface of the projectile was a mixture of air and vapor. The smaller the inner diameter, the less air and the more vapor there is on the outer surface of the projectile.

When hollow projectiles with four apertures enter the water at a velocity of 100 m/s, the vapor moves continuously upward from the head of the cavity, and the cavitation at the tail of the cavity gradually decreases with the contraction of the cavity. With an increase in the cavity size, the vapor content in the cavity gradually increased, and the cavitation became more obvious. The smaller the inner diameter of the hollow projectile, the larger the cavity produced, the more obvious the cavitation, and the higher the amount of vapor generated.

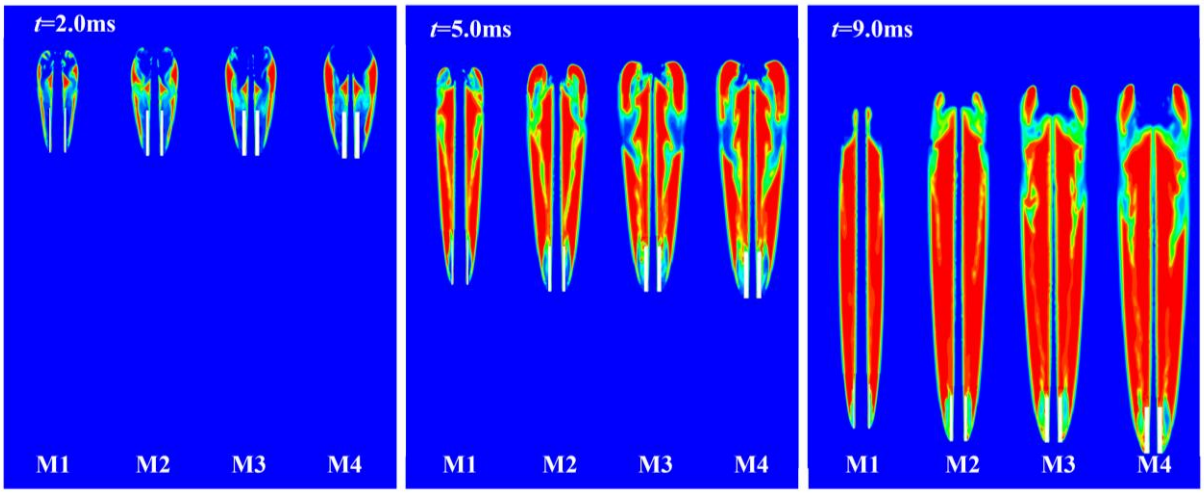


**Fig. 15 Vapor volume fraction at different aperture sizes**

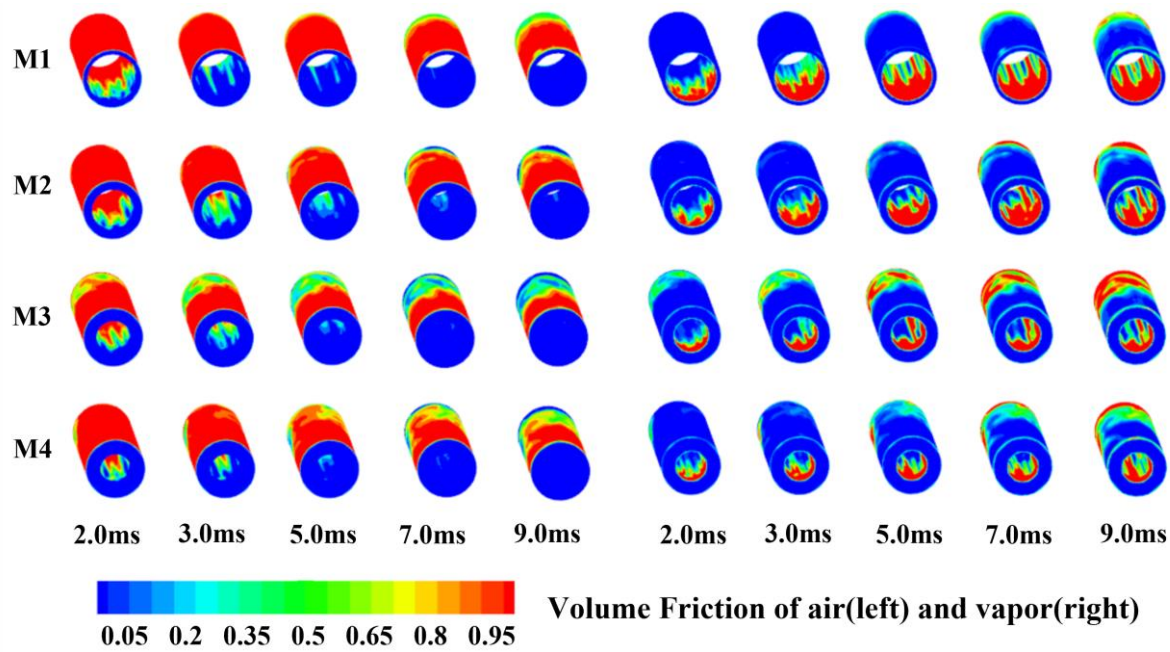


**Fig. 16 Wetting diagram of air and vapor at different aperture sizes**

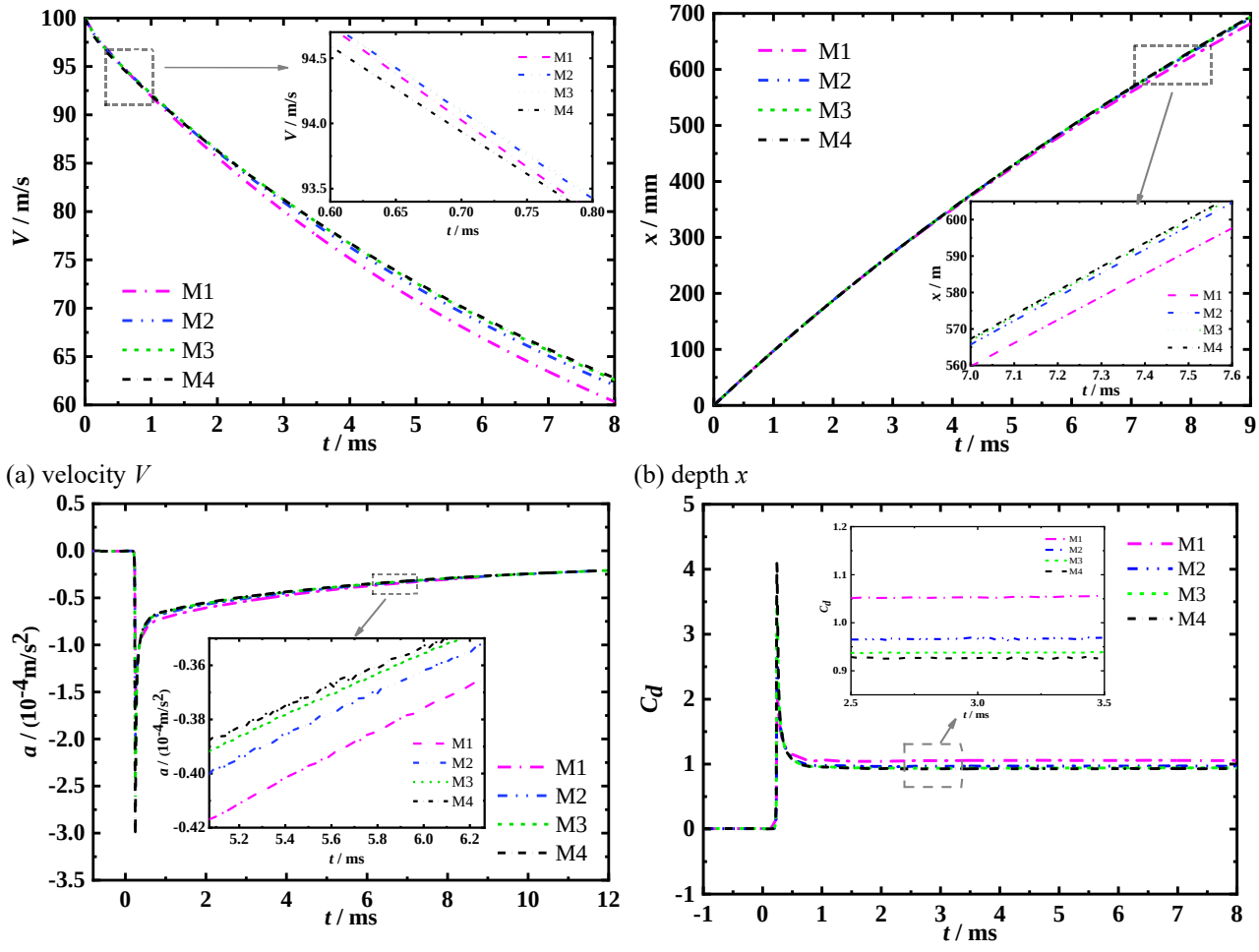


(a) velocity $V$ (b) depth $x$

(c) Acceleration $a$ (d) Drag coefficient $C_d$

**Fig. 17 Change process of motion parameters and resistance of four hollow projectiles**

### 3.2.3 Analysis of Hydrodynamics and Motion Characteristics of Projectile

Figure 17. shows the change in the motion characteristics and resistance coefficient of the four hollow projectiles when they enter the water at a velocity of 100 m/s. By comparison, it is found that the size of the

hollow projectile aperture has less influence on the motion process of the projectile, and the trends of the motion characteristics and resistance coefficient are basically similar. The main difference is that the contact area with the water surface is different when projectiles of different apertures enter the water, thereby resulting in a large difference in the resistance coefficient and change in the motion parameters. As shown in Fig. 17(a), the velocity of M4 with the smallest aperture decreases the fastest until $t$=0.8 ms. After $t$=0.8 ms, the velocity drops of the projectile with aperture M4 and M1 gradually slows down and accelerates, respectively. At 8 ms, the velocity reduction was the greatest for M1 and the least for M4. This was owing to the rapid collision of the hollow projectile head with the water surface when it entered the water. The smaller aperture of M4 produces greater resistance. As such, the initial velocity drops at the fastest rate. Owing to the larger mass of M4 under similar velocity conditions, the kinetic energy generated is greater than that of M1. Hence, the velocity decreases more slowly after completely entering the water, and that of M1 decreases faster after completely entering the water. As shown in Fig. 17(b), the displacements of the hollow projectiles of different aperture sizes moving simultaneously are essentially similar. The projectile with aperture M4 had the greatest displacement, and that with aperture M1 had the least displacement simultaneously, which can be explained by the velocity curves.

As shown in Fig. 17(c), the peak acceleration of the M4 projectile at the time of the projectile impact on the water surface is the largest, and that of the M1 projectile is the smallest. Further, the acceleration immediately decreases and keeps fluctuating with time owing to the high velocity of the projectile. A mixture of vapor and air is produced in the cavity, while the motion of the gas hitting the wall of the projectile causes the acceleration to fluctuate. The acceleration of different apertures is essentially similar at 12 ms. Before 12 ms, the acceleration of the M1 and M4 projectiles are the largest and smallest, respectively, which can explain the fastest decrease in the velocity and shortest displacement of the motion of M1. As shown in Fig. 17(d), at the time of impact, the resistance coefficient increased to its maximum value and decreased immediately. Owing to the small pore size and large wetted area of M4, the resistance of M4 is the largest. However, the resistance coefficient of M4 is the smallest, while the in-resistance coefficient of M1 is the largest.

In summary, when the bore diameter decreases, the drag coefficient of the projectile decreases, the velocity decays faster at the moment of water entry, and the acceleration decreases. However, at a later stage, the acceleration of the hollow projectiles with different bore diameters remains essentially similar.

Figure 18 shows the frictional resistance of the hollow projectile with different apertures. At the early stage of water entry, the frictional resistance of the projectile is consistent with the previous description of different velocities with two-step points. There is little difference in the frictional resistance of M1 and M2, and at 3.5–7 ms, it is obvious from the graph that M1 has less resistance. There is also little difference in the frictional

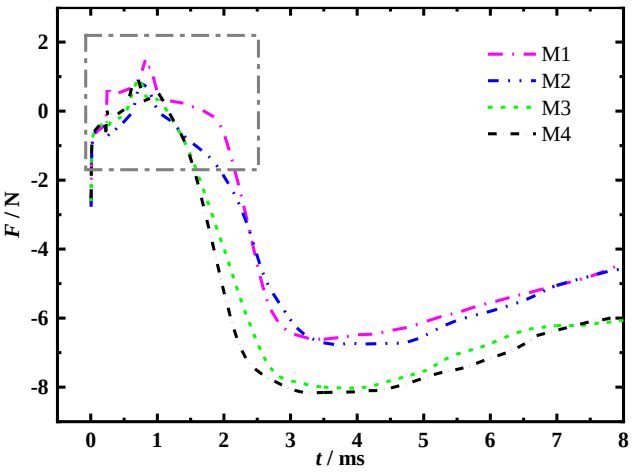


(a) Variation of frictional resistance from 0-8 ms

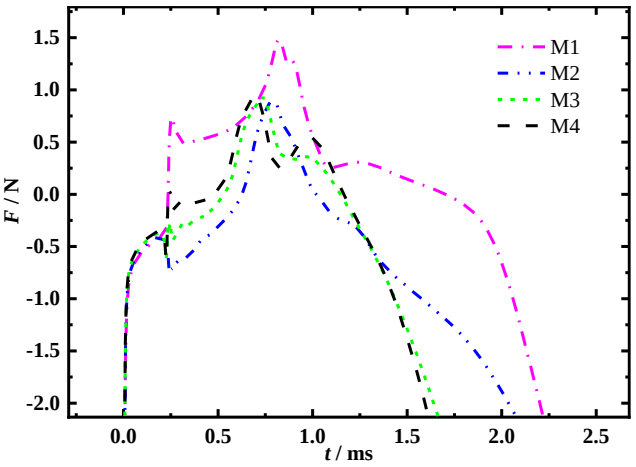


(b) Variation of the frictional resistance from 0–2.6 ms

**Fig. 18 Frictional resistance of the hollow projectiles with different apertures**

resistance of M3 and M4, and at 1.5–7 ms, M3 has less frictional resistance and is equal to M4 at 7 ms. When combined gas and water produce similar frictional resistance, the frictional resistance of projectiles M1 and M2 has three intersection points at 2.4, 3.3, and 7.4 ms. Projectiles M3 and M4 have one intersection at 7.4 ms. Projectile M4 has the smallest inner diameter and surface area of the projectile body. However, because it is wetted with a majority of the water, it produces the largest frictional resistance. In summary, after the hollow projectile is stabilized in water, the aperture ratio ranges from 0.51 to 0.83. The smaller the aperture ratio, the higher the frictional resistance of the hollow projectiles.

## 4. CONCLUSION

In this study, the processes of high-speed vertical water entry of hollow projectiles were studied using numerical simulation. The effects of the different water entry speeds and aperture diameters on the cavity morphology, cavitation characteristics, hydrodynamics, and motion characteristics of the hollow projectile were investigated separately. Additionally, the effect of the frictional resistance on the motion of the hollow projectile was analyzed in detail. The following conclusions were

obtained.

When the hollow projectile entered the water at different speeds, as the speed increased, the larger the cavity, the more obvious the cavitation phenomenon, and the wetter the hollow projectile. However, the timing of the surface closure of the cavity changes. At 50 m/s, the cavity closed during contraction, and at 100–200 m/s, the cavity closed during stretching. As the speed of entry into the water increases, the speed of decay becomes higher, thereby increasing the displacement of the movement. At 50 m/s, the drag coefficient of the projectile was greater than those of the other three projectile velocities.

When hollow projectiles with different apertures enter the water at a similar speed (as the inner diameter decreases), the larger the diameter of the resulting cavity and the more vapor is produced by cavitation. However, there was less air on the outer surface of the hollow projectile, thereby making the wetting more obvious. During the contraction of the cavity, the degree of contraction became apparent as the inner diameter increased. When the diameter of the aperture is reduced, the resistance of the projectile increased, although the acceleration and drag coefficient decreased. The speed decayed faster at the moment of impact. However, after entering the water, the acceleration was reduced, the speed decayed at a lower rate, and the displacement was longer.

During the motion of the projectile, the frictional resistance has step points when the projectile impacts the water surface and completely enters the water. The higher the initial speed, the earlier the step point, and the greater the frictional resistance of the projectile. When the aperture ratio varies from 0.51 to 0.83, the frictional resistance also has two step points, and the frictional resistance is not significantly different. The smaller the aperture ratio, the higher the frictional resistance of the hollow projectile.

## ACKNOWLEDGEMENTS

This research was supported by the National Natural Science Foundation of China (No. 12002165), the Major Fundamental Research Project (909120704), Quick Support (80907020304) of the Equipment Development Department, the Nature Science Youth Foundation of Jiangsu Province (No. BK20210348), and the National Key Laboratory Foundation of Transient Physics (No. 6142604210603). We are grateful for this support.

## CONFLICT OF INTEREST

The authors declare that they have no conflicts of interest.

## AUTHORS CONTRIBUTION

All authors contributed to the conception and design of the study. Haowei Fan and Hao Wang performed numerical simulations. Haowei Fan wrote the initial draft of the manuscript. Hao Wang and Xiangyan Liu participated in the revision of the first and final drafts. Zhengui Huang and Zhihua Chen validated the results and reviewed the original draft of this paper. Fujun Xiao and Rongxian Qiu processed the data.

## REFERENCES

Akbari, M. A., Mohammadi, J., & Fereidooni, J. (2020). Stability of oblique water entry of cylindrical projectiles. *Journal of Applied Fluid Mechanics*, 14(1), 301-314. https://doi.org/10.47176/jafm.14.01.31682

Chen, T., Huang, W., Zhang, W., Qi, Y., & Guo, Z. (2019). Experimental investigation on trajectory stability of high-speed water entry projectiles. *Ocean Engineering*, 175, 16-24. https://doi.org/10.1016/j.oceaneng.2019.02.021

Du, H., Jiang, F., Huang, Z., Chen, Z., & Sun, X. (2018). Simulation of critical inlet angle of inner conical hollow projectile under choke flow. *Journal of Nanjing University of Science and Technology,* (6). https://doi.org/10.14177/j.cnki.32-1397n.2018.42.06.002

Erfanian, M. R., & Anbarsooz, M. (2018). Numerical investigation of body and hole effects on the cavitating flow behind a disk cavitator at extremely low cavitation numbers. *Applied Mathematical Modelling*, 62, 163-180. https://doi.org/10.1016/j.apm.2018.05.026

Hou, Y., Huang, Z., Chen, Z., Guo, Z., & Han, L. (2021). Different closure patterns of the hollow cylinder cavities with various water-entry velocities. *Ocean Engineering*, 221, 108526. https://doi.org/10.1016/j.oceaneng.2020.108526

Hou, Y., Huang, Z., Guo, Z., Chen, Z., Liu, R., & Luo, Y. (2020). Experimental investigation on shallow-angle oblique water-entry of a high-speed supercavitating projectile. *Acta Armamentarii*, 41(2), 332. https://doi.org/10.1016/j.jfluidstructs.2021.103305

Hu, X., Wei, Y., & Wang, C. (2023). Hydrodynamics of the projectile entering the water under the ice hole constraint environment. *Physics of Fluids*, 35(4). https://doi.org/10.1063/5.0146980

Huang, Z., Li, Y., Chen, Z., & Guo, Y. (2013). Numerical investigations on the drag and aerodynamic characteristics of a hollow projectile. *Acta Armamentarii*, 34(5), 535. https://doi.org/10.3969/j.issn.1000-1093.2013.05.004

Huang, Z., Wang, R. Chen, Z., Hou, Y., & Luo, Y. (2018). Experimental study of cavity characteristic induced by vertical water entry impact of a projectile with a 90 cone-shaped head at different velocities. *Explosion and Shock Waves*, 38(6), 1189-1199. http://doi.org/10.11883/bzycj-2018-0115

Jafari, M. A., & Akbarzadeh, P. (2022). Experimental analysis of water entry problem considering hollow cylinders: The impact of hole geometry. *Ocean Engineering*, 259, 111906. https://doi.org/10.1016/j.oceaneng.2022.111906

Liu, H., Zhou, B., Yu, J., Liu, K., Han, X., & Zhang, G. (2023). Experimental investigation on the multiphase flow characteristics of oblique water entry of the hollow cylinders. *Ocean Engineering*, 272, 113902. https://doi.org/10.1016/j.oceaneng.2023.113902

Liu, S., Wang, Z., Li, L., & Zhang, M. (2023). The influence of nose Shape on the stability of projectile entering water at high speed. *Acta Aeronautica et Astronautica Sinica*, 40(X), 28437. https://doi.org/10.7527/S1000-6893.2023.28437

Luo, Y., Huang, Z., Chen, Z., Hou, Y., & Guo, Z. (2019). *Experimental Study on the Effect of Head Cone Angle on the Low Velocity Oblique Inlet Process of Projectile.* 31st International Symposium on Ballistics. http://doi.org/10.12783/ballistics2019/33209

Ma, Q., He, C., Wang, C., Wei, Y., Lu, Z., & Sun, J. (2014). Experimental investigation on vertical water-entry cavity of sphere. *Explosion And Shock Waves*, 34(2), 174-180. http://doi.org/10.11883/1001-1455(2014)02-0174-07

Mu, Q., Lv, Y., Wang, K., Xiong, T., & Yi, W. (2019). Numerical simulation on the cavitation flow of high speed oblique water entry of revolution body. *Mathematical Problems in Engineering*, 2019, 1-10. https://doi.org/10.1155/2019/8034619

Qian, J., Li, Y., Chen, Z., & Yi, W. (2011). The investigation on flow characteristics of a low-drag hollow projectile. *Danjian yu Zhidao Xuebao/ Journal of Projectiles, Rockets, Missiles and Guidance*, 31(4). https://doi.org/10.15892/j.cnki.djzdxb.2011.04.051

Quan, X., Zhang, H., Ma, T., Zhang, Y., & Wu, Y. (2021). Simulation research on critical area ratio of throat to entrance of inner conical hollow projectile under choke flow. *Journal of Ordnance Equipment Engineering*, 42(04), 97-101. https://doi.org/10.11809/bqzbgcxb2021.04.018

Savchenko, G. Y. (2011). *Hydrodynamic characteristics of a disc with central duct in a supercavitation flow*. In Supercavitation: Advances and Perspectives A collection dedicated to the 70th jubilee of Yu. N. Savchenko. Berlin, Heidelberg: Springer Berlin Heidelberg. https://doi.org/10.1007/978-3-642-23656-3_6

Shi, Y., Wang, G., & Pan, G. (2019). Experimental study on cavity dynamics of projectile water entry with different physical parameters. *Physics of Fluids*, 31(6). https://doi.org/10.1063/1.5096588

Wang, R., Huang, Z., & Zhu, S. (2017). Experimental and numerical study of cavity closure of flat projectile entering water. *Journal of Ordnance Equipment Engineering*, 12, 36-39. http://doi.org/10.11809/scbgxb2017.12.009

Wang, X., & Lyu, X. (2021). Experimental study on vertical water entry of twin spheres side-by-side. *Ocean Engineering*, 221, 108508. https://doi.org/10.1016/j.oceaneng.2020.108508

Wang, Y. (1996). Studying progress on hollow projectile technique in the western countries. *Projectile and Rocket Technology*, 1(3), 14-23.

Wessam, M. E., Huang, Z., & Chen, Z. (2014). *Aerodynamic characteristics and flow field investigations of an optimal hollow projectile.* Proceedings of the 5th International Conference on Mechanical Engineering and Mechanics. http://doi.org/10.13140/2.1.2037.9529

Worthington, A. M., & Cole, R. S. (1897). V. Impact with a liquid surface, studied by the aid of instantaneous photography. *Philosophical Transactions of the Royal Society of London. Series A, Containing Papers of a Mathematical or Physical Character*, (189), 137-148. https://doi.org/10.1098/rsta.1897.0005

Xie, W., Yang, M., & Gong, J. (2019). Underwater attack-defense confrontation system and its future development. *Strategic Study of Chinese Academy of Engineering*, 21(6), 71-79. https://doi.org/10.15302/J-SSCAE-2019.06.014

Yun, H., Lyu, X., & Wei, Z. (2020). Experimental study on vertical water entry of two tandem spheres. *Ocean Engineering*, 201, 107143. https://doi.org/10.1016/j.oceaneng.2020.108508

Zhang, H., Wen, Q., Wang, Y., & Zhang, Z., (2016). Theoretical calculations and numerical simulation on air resistance characteristics of hollow projectile. *Journal of Ordnance Equipment Engineering*, 2016(7), 5-11. https://doi.org/10.11809/scbgxb2016.07.002

Zhao, Q., & Chen, Z. (2017). Numerical optimization of aerodynamic configuration of a hollow projectile based on the approximation model. *Acta Aerodynamica Sinica*, 35(3), 408-414. http://doi.org/10.7638/kqdlxxb-2015.0056

Zhao, Q., Chen, Z. H., Huang, Z. G., Zhang, H. H., & Ma, J. (2019). Optimization of the aerodynamic configuration of a tubular projectile based on blind kriging. *Scientia Iranica*, 26(1), 311-322. https://doi.org/10.24200/sci.2017.20015

Zhou, D., & Shi, H. (2022). Numerical simulation of cavitation and motion characteristics of high-speed water entry of tandem revolved bodies. *Chinese Journal of Applied Mechanics*, 39(6), 1168-1177. https://doi.org/10.11776/j.issn.1000-4939.2022.06.018